# Supplementary Information: Evidence for Isotropic s-Wave Superconductivity in High-Entropy Alloys

Casey K.W. Leung,[1] Xiaofu Zhang,[2,3] Fabian von Rohr,[4] Rolf Lortz,[1,5] and Berthold Jäck[1,5]

[1] *Department of Physics, The Hong Kong University of Science and Technology, Clear Water Bay, Kowloon, Hong Kong SAR*
[2] *State Key Laboratory of Functional Materials for Informatics, Shanghai Institute of Microsystem and Information Technology, Chinese Academy of Sciences (CAS), Shanghai 200050, China*
[3] *CAS Center for Excellence in Superconducting Electronics, Shanghai 200050, China*
[4] *Department of Chemistry, Universiät Zürich, Winterthurerstrasse 190, 8057 Zurich, Switzerland*
[5] *IAS Center for Quantum Technologies, The Hong Kong University of Science and Technology, Clear Water Bay, Kowloon, Hong Kong SAR*

(Dated: June 21, 2022)

## Appendix A: Structural and chemical properties of the $(TaNb)_{1-x}(ZrHfTi)_x$ thin films

### 1. Calculation of binary enthalpies

The binary mixing enthalpies of Ta, Nb, Zr, Hf, and Ti are summarized in Table I. The binary mixing enthalpies of Ta-Nb, Zr-Hf, Zr-Ti, and Hf-Ti are all zero that is they neither attract nor repel each other, but mix ideally. The binary mixing enthalpies of other two-element configurations show small positive values that would favor segregation upon long-term annealing. However, the high-entropy alloy (HEA) films investigated in this study are fabricated by using magnetron sputtered at ambient temperatures without post-annealing. Because of the the high mixing entropy, random elemental mixing into a crystalline single phase is favored over possible multi-phase segregation. Consistent with our previous work [1], this understanding is corroborated by our energy-dispersive X-ray spectroscopy and X-ray diffraction measurements presented in the following sub-section. Results from these measurements show a complete elemental mixing and a single phase crystallizing on the body-centered cubic lattice.

TABLE I: Binary mixing enthalpies (in kJ/mol) for unlike atom pairs constituting the $(TaNb)_{1-x}(ZrHfTi)_x$ alloy.

| | | | | |
|---|---|---|---|---|
| Ta | 0 | 3 | 3 | 1 |
| 0 | Nb | 4 | 4 | 2 |
| 3 | 4 | Zr | 0 | 0 |
| 3 | 4 | 0 | Hf | 0 |
| 1 | 2 | 0 | 0 | Ti |

### 2. Structural and chemical characterizations

The structural and chemical properties of the $(TaNb)_{1-x}(ZrHfTi)_x$ alloy were characterized by using x-ray diffraction (XRD) and energy-dispersive x-ray spectroscopy (EDX) with the scanning electron microscope (SEM), respectively.

Using EDX measurements we have characterized the precise stoichiometric composition of the nominal $x = 0.40$ and $x = 0.75$ films. The relative concentrations of the various elements are listed in Table II. The resulting compositions $x = 0.35$ and $x = 0.71$ closely match the nominal composition targeted during sputter deposition. Spatial EDX mapping conducted on both films, furthermore, reveals a uniform spatial distribution of the five constituent elements of the $(TaNb)_{1-x}(ZrHfTi)_x$ alloy (see Fig. A.1(a) and (b)). This finding reflects the random elemental mixing at the atomic level characteristic for HEAs and is consistent with previous reports [1, 2].

We have conducted 2-$\Theta$ XRD scans of the $x = 0.35$ and $x = 0.71$ samples. Fig. A.2 shows the resulting XRD spectrum for measurements on the $x = 0.71$ film using a Cu K(alpha) X-ray source. The diffraction peaks can be labelled with the indices of a body-centered cubic lattice for films at both alloy compositions. The observation of a bcc lattice structure is consistent with previous reports on films and bulk crystals of this material [1, 2].

TABLE II: SEM-EDX analysis of the relative atomic concentrations of the constituent chemical elements of the nominal $x = 0.40$ and $x = 0.75$ films.

| Element | Atomic % for $x = 0.40$ film (±0.01%) | Atomic % for $x = 0.75$ film (±0.01%) |
|---|---|---|
| Ti | 10.37 | 23.33 |
| Zr | 10.32 | 21.60 |
| Nb | 31.99 | 14.28 |
| Hf | 14.49 | 26.74 |
| Ta | 32.82 | 14.04 |

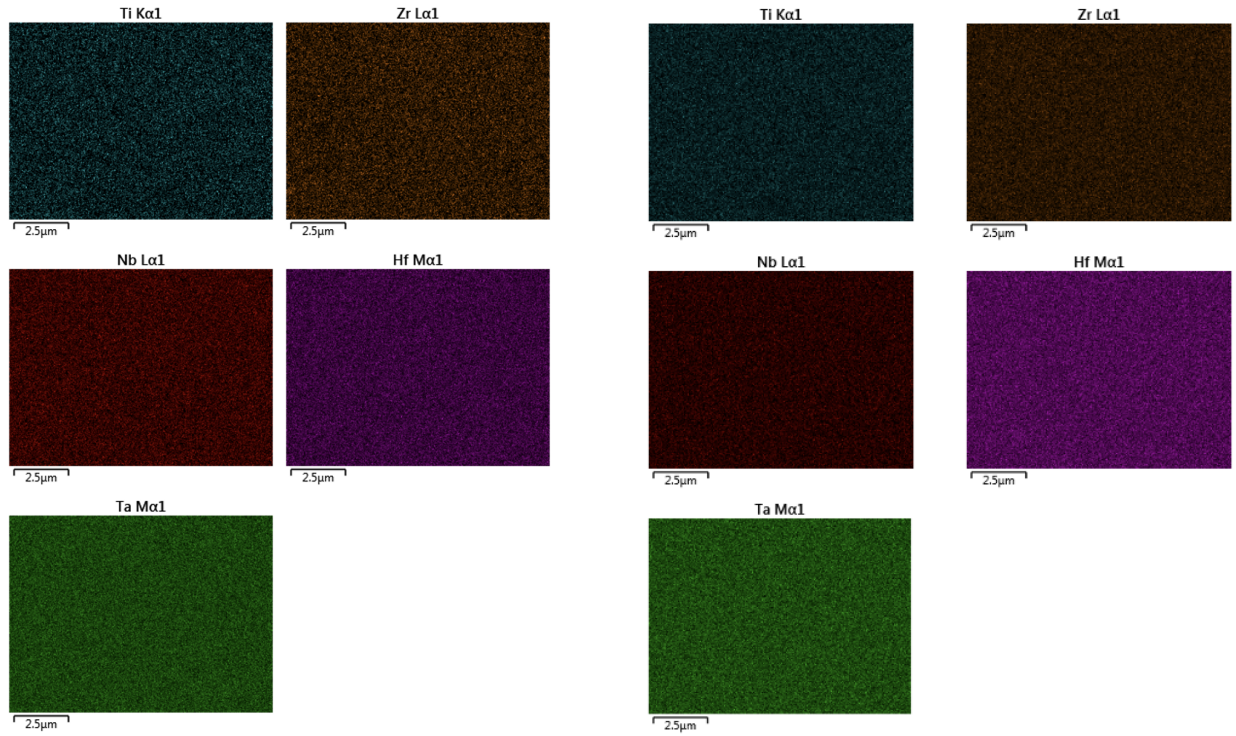


FIG. A.1: (a) and (b) show spatial maps of the relative atomic concentration for the various constituent elements of the $x = 0.35$ and $x = 0.71$ films, respectively.

### Appendix B: Measurements of the magnetic susceptibility of the $x = 0.71$ film

We present the measured magnetic field dependence of $-4\pi M$ measured at various temperatures for the $x = 0.71$ film in Fig. B.1. The magnetic field has been applied in the sample plane along two orientations rotated by 45 °. We have analyzed $-4\pi M(H,T)$ as described in the main text and the resulting $H_{c1}$ values are shown in Fig. 1(d). In Fig. B.2, we show measurements of $-4\pi M$ for a larger range of the external magnetic field applied perpendicular to the sample plane at various representative temperatures. Deviations of $-4\pi M(H)$ from a linear background can be used for determining $H_{c2}$ as described in the main text. The resulting $H_{c2}(T)$ is shown in Fig. 2(b) of the main text.

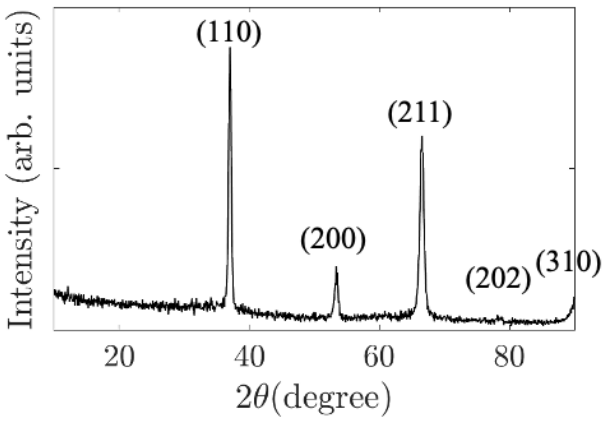


FIG. A.2: X-ray diffraction spectrum of a 2-Θ scan of the $x = 0.71$ film.

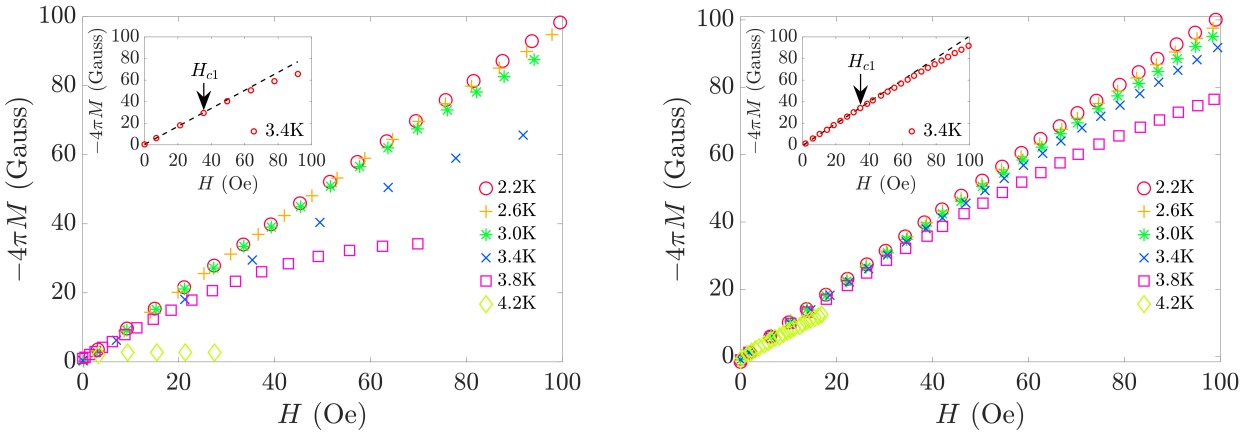


FIG. B.1: Measurements of $-4\pi M(H)$ at various indicated temperatures for the $x = 0.71$ film for extracting $H_{c1}$ with the magnetic field $H$ applied along two angles 0° (a) and 45° (b) within the sample plane.

### Appendix C: Sample volume for calculation of volume magnetization $M$

The samples are cut with dimension $a \times b \times c = 2.15 \pm 0.01 \times 2.90 \pm 0.01 \times 0.0011 \pm 0.0001\,\mathrm{mm}^3$ and $2.61 \pm 0.01 \times 2.23 \pm 0.01 \times 0.0010 \pm 0.0001\,\mathrm{mm}^3$ for $x = 0.35$ and $x = 0.71$, respectively. The volume magnetization $-4\pi M$ can be calculated from the magnetic susceptibility $\chi$ using $-4\pi M = 4\pi\chi/V$ with $V = a \times b \times c$ as the sample volume.

### Appendix D: Determination of the lower critical field $H_{c1}$

$H_{c1}$ can be determined by analysing the magnetic field $H$ dependence of $-4\pi M$. Upon the application of an external magnetic field $0 < H < H_{c1}$, the superconductor displays a diamagnetic response, which is characterised by a linear $-4\pi M(H)$. Once vortices start to enter the superconducting bulk at $H = H_{c1}$, $-4\pi M(H)$ becomes non-linear for increasing field strengths $H > H_{c1}$.

A linear least-square fit to the diamagnetic response at $H < H_{c1}$ can be used to accurately determine $H_{c1}$ given adequate experimental data quality. Analysing the resulting Pearson coefficient $R^2$ as shown in Fig. D.1, we can extract $H_{c1}$ as the field at which $R^2 < 1$.

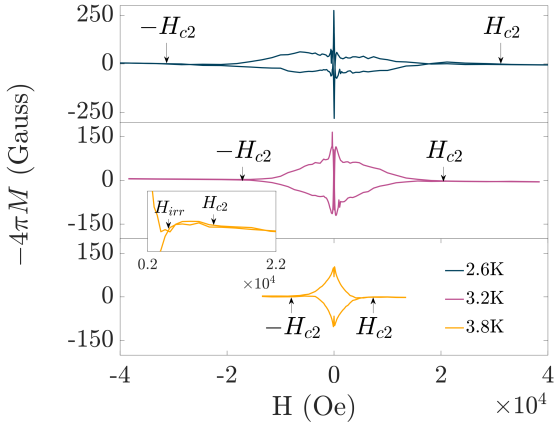


FIG. B.2: Measurements of $-4\pi M(H)$ at representative temperatures of the $x = 0.71$ film over a larger field range for determining $H_{c2}$, as shown in the inset. $H_{\mathrm{irr}}$ denotes the irreversibility field.

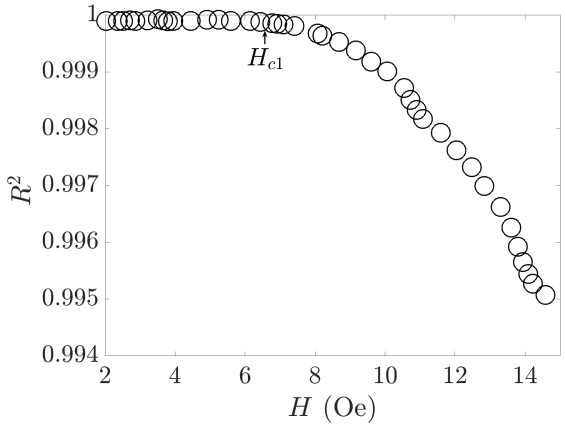


FIG. D.1: The Pearson correlation $RR$ of a linear fit to $-4\pi M(H)$ is plotted. $H_{\mathrm{c1}}$ is determined as the field $H$ at which $RR < 1$. An example for $x = 0.35$ and $T = 4\,\mathrm{K}$ is shown.

### Appendix E: Complete list of determined physical parameters through the analysis of $M(H,T)$

All material parameters that were extracted via the analysis of $-4\pi M(H,T)$ are shown in Table III and IV for the $x = 0.35$ and $x = 0.71$ film, respectively.

TABLE III: Physical parameters of the $x = 0.35$ film. $T$ denotes the temperature, $H_{c1}$ the lower critical field, $H_{c2}$ the upper critical field, $\xi$ the Ginzburg-Landau coherence length, $\lambda$ the penetration depth, and $\kappa$ the Ginzburg-Landau parameter.

| $T$(K) | $H_{c1}$(Oe) (±0.3) | $H_{c2}$(Oe) (±1600) | $\xi$(nm) (±0.2) | $\lambda$(nm) | $\kappa = \lambda/\xi$ |
|---|---|---|---|---|---|
| 2.2 | 9.8 | 67900 | 7.0 | 903.32 | 129.60 |
| 2.4 | 9.6 | 65100 | 7.1 | 913.63 | 128.32 |
| 2.6 | 9.2 | 62300 | 7.3 | 929.99 | 127.92 |
| 2.8 | 8.8 | 60600 | 7.4 | 953.24 | 128.30 |
| 3 | 8.4 | 57800 | 7.6 | 977.55 | 128.46 |
| 3.2 | 8.2 | 54600 | 7.8 | 985.85 | 126.23 |
| 3.4 | 7.8 | 52200 | 8.0 | 1013.24 | 126.81 |
| 3.6 | 7.4 | 48500 | 8.3 | 1038.34 | 125.25 |
| 3.8 | 7.2 | 45500 | 8.6 | 1044.8 | 122.06 |
| 4 | 6.9 | 43500 | 9.1 | 1064.21 | 116.56 |
| 4.2 | 6.7 | 40100 | 9.5 | 1083.07 | 114.01 |
| 4.4 | 6.3 | 37100 | 9.9 | 1106.69 | 111.56 |
| 4.6 | 5.8 | 33500 | 10.4 | 1161.17 | 111.65 |
| 4.8 | 5.4 | 29800 | 11.1 | 1198.56 | 108.17 |
| 5 | 4.7 | 26800 | 11.8 | 1277.66 | 108.64 |
| 5.2 | 4.4 | 23800 | 12.8 | 1319.05 | 103.29 |
| 5.4 | 3.9 | 20800 | 13.9 | 1405.63 | 101.34 |
| 5.6 | 3.1 | 18500 | 15.1 | 1559.53 | 103.21 |
| 5.8 | 2.5 | 14400 | 17.3 | 1728.42 | 100.20 |
| 6 | 2.3 | 11700 | 19.8 | 1805.33 | 91.09 |
| 6.2 | 1.8 | 7000 | 25.6 | 2028.80 | 79.31 |
| 6.4 | 1.1 | 5000 | 37.5 | 2548.68 | 68.04 |

TABLE IV: Physical parameters of the $x = 0.71$ film. $T$ denotes the temperature, $H_{c1}$ the lower critical field, $H_{c2}$ the upper critical field, $\xi$ the Ginzburg-Landau coherence length, $\lambda$ the penetration depth, and $\kappa$ the Ginzburg-Landau parameter.

| $T$(K) | $H_{c1}$(Oe)(0°) (±3) | $H_{c1}$(Oe)(45°) (±3) | $H_{c2}$(Oe) | $\xi$(nm) | $\lambda$(nm) | $\kappa = \lambda/\xi$ |
|---|---|---|---|---|---|---|
| 2.2 | 76 | 74 | 46500 (±6000) | 8.42 | 275.5 | 32.72 |
| 2.4 | 70 | 62 | 41600 (±2000) | 8.90 | 285.2 | 32.05 |
| 2.6 | 65 | 62 | 38500 (±2000) | 9.63 | 295.2 | 30.65 |
| 2.8 | 59 | 58 | 33100 (±5000) | 9.98 | 310.3 | 31.09 |
| 3 | 52 | 50 | 28503 (±5000) | 10.48 | 331.8 | 31.66 |
| 3.2 | 50 | 42 | 24538 (±3000) | 12.50 | 329.3 | 26.34 |
| 3.4 | 35 | 35 | 21126 (±3000) | 14.49 | 391.7 | 27.03 |
| 3.6 | 29 | 27 | 15658 (±3000) | 16.85 | 430.5 | 25.55 |
| 3.8 | 23 | 18 | 11606 (±200) | 19.56 | 481.0 | 24.59 |
| 4 | 11 | 10 | 6375 (±700) | 24.47 | 725.8 | 29.66 |
| 4.2 | 3 | 3 | 2596 (±300) | 35.60 | 1346.5 | 37.82 |

[1] X. Zhang, N. Winter, C. Witteveen, T. Moehl, Y. Xiao, F. Krogh, A. Schilling, and F. von Rohr, Phys. Rev. Res. **2**, 013375 (2020).

[2] V. Rohr, Fabian, Winiarski, M. J, Tao, Jing, Klimczuk, Tomasz, Cava, and R. Joseph, Proceedings of the National Academy of Sciences **113**, E7144 (2016).